Structure–function analyses of the ion channel TRPC3 reveal that its cytoplasmic domain allosterically modulates channel gating

Received for publication, July 25, 2018, and in revised form, August 17, 2018 Published, Papers in Press, August 23, 2018, DOI 10.1074/jbc.RA118.005066

Francisco Sierra-Valdez[‡1], Caleigh M. Azumaya[§1], Luis O. Romero[‡], Terunaga Nakagawa[§¶‖2,3], and Julio F. Cordero-Morales[‡2,4]

From the [‡]Department of Physiology, University of Tennessee Health Science Center, Memphis, Tennessee 38163 and [§]Department of Molecular Physiology and Biophysics, [¶]Center for Structural Biology, and [‖]Vanderbilt Brain Institute, Vanderbilt University School of Medicine, Nashville, Tennessee 37232

Edited by Karen G. Fleming

The transient receptor potential ion channels support Ca^{2+} permeation in many organs, including the heart, brain, and kidney. Genetic mutations in transient receptor potential cation channel subfamily C member 3 (TRPC3) are associated with neurodegenerative diseases, memory loss, and hypertension. To better understand the conformational changes that regulate TRPC3 function, we solved the cryo-EM structures for the full-length human TRPC3 and its cytoplasmic domain (CPD) in the apo state at 5.8- and 4.0-Å resolution, respectively. These structures revealed that the TRPC3 transmembrane domain resembles those of other TRP channels and that the CPD is a stable module involved in channel assembly and gating. We observed the presence of a C-terminal domain swap at the center of the CPD where horizontal helices (HHs) transition into a coiled-coil bundle. Comparison of TRPC3 structures revealed that the HHs can reside in two distinct positions. Electrophysiological analyses disclosed that shortening the length of the C-terminal loop connecting the HH with the TRP helices increases TRPC3 activity and that elongating the length of the loop has the opposite effect. Our findings indicate that the C-terminal loop affects channel gating by altering the allosteric coupling between the cytoplasmic and transmembrane domains. We propose that molecules that target the HH may represent a promising strategy for controlling TRPC3-associated neurological disorders and hypertension.

The transient receptor potential (TRP)[5] ion channels support Ca^{2+} permeation in a variety of tissues, including, but not restricted to, those of the heart, brain, and kidney (1, 2). The 27 mammalian TRP channels are classified under six subfamilies, TRPC (canonical), TRPM (melastatins), TRPV (vanilloid), TRPA (ankyrin), TRPML (mucolipins), and TRPP (polycystins) based on primary structure similarity (2). Inherited mutations in TRP channels underlie numerous pathological conditions, such as peripheral neuropathies, heart failure, cardiac arrhythmia, and pulmonary hypertension (3). The TRPC ion channels consist of seven members, TRPC1–7. They are further divided into three groups based on sequence similarity and functional analyses: TRPC1/4/5 are activated by $G\alpha_q$-coupled receptors and receptor tyrosine kinases, whereas TRPC3/6/7 are activated by diacylglycerol (DAG). TRPC2 is a pseudogene (2). A relevant feature of the TRPC subfamily is that its members can form homo- and heterotetramers (4, 5); hence, TRPC physiological and biophysical properties might be broader in hetero-multimeric assemblies (6).

TRPC3 is expressed in the Purkinje cells and unipolar brush cells in the cerebellum (7, 8). It regulates neuronal excitability in a circuit essential for behaviors related to motor learning and coordination. Indeed, a gain-of-function mutant in the TRPC3

This work was supported by National Institutes of Health Grant R01 HD061543, the Vanderbilt University Trans-Institutional Program, and other internal funding (to T. N.); American Heart Association Grant 15SDG25700146 and National Institutes of Health Grant 1-R01GM125629-01 (to J. C.-M.); and National Institutes of Health Molecular Biophysics Training Program Grant T32 GM008320 to Walter Chazin (to C. M. A.). The authors declare that they have no conflicts of interest with the contents of this article. The content is solely the responsibility of the authors and does not necessarily represent the official views of the National Institutes of Health.

This article contains Figs. S1–S8.

The atomic coordinates and structure factors (codes 6D7L, 6DJR, and 6DJS) have been deposited in the Protein Data Bank (http://wwpdb.org/).

The EM density maps have been deposited in the EMDataBank under accession codes EMD-7823 and EMD-7940.

[1] Both authors contributed equally to this work.

[2] Co-senior authors.

[3] To whom correspondence may be addressed: Dept. of Molecular Physiology and Biophysics, Vanderbilt Brain Institute, Center for Structural Biology, Vanderbilt University School of Medicine, 702 Light Hall, Nashville, TN 37232-0615. Tel.: 615-875-2531; E-mail: terunaga.nakagawa@vanderbilt.edu.

[4] To whom correspondence may be addressed: Dept. of Physiology, University of Tennessee Health Science Center, Memphis, TN 38163. Tel.: 901-448-8206; E-mail: jcordero@uthsc.edu.

[5] The abbreviations used are: TRP, transient receptor potential; CPD, cytoplasmic domain; HH, horizontal helix; TRPC, canonical transient receptor potential; TRPM, melanin transient receptor potential; TRPV, vanilloid transient receptor potential; TRPA, ankyrin transient receptor potential; TRPML, mucolipin transient receptor potential; TRPP, polycystin transient receptor potential; DAG, diacylglycerol; S, segment; cryo-EM, cryogenic electron microscopy; MBP, maltose-binding protein; LHD, linker helical domain; LH, linker helix; CaM, calmodulin; CIRB; calmodulin (CaM)/IP_3 receptor–binding site; Sf9, *Spodoptera frugiperda* Sf21; GDN, glyco-diosgenin; TMD, transmembrane domain; RELION, regularized likelihood optimization; DDM, dodecyl maltoside; PMAL-C8, poly(maleic anhydride-*alt*-1-decene) substituted with 3-(dimethylamino)propylamine; VH, vertical helix; ARD, ankyrin repeat domain; AR, ankyrin repeat; GSK-170, GSK-1702934A; TCEP, tris(2-carboxyethyl)phosphine; TEV, tobacco etch virus; CTF, contrast transfer function; NCS, non-crystallographic symmetry; FSC, Fourier shell correlation; IP_3, inositol 1,4,5-trisphosphate; HEK, human embryonic kidney; hTRPC, human TRPC; pix, pixel; Cs, spherical aberration.

S4–S5 linker region (T573A) causes abnormal Purkinje cell development and cerebellar ataxia (*i.e.* inability to coordinate balance, gait, extremities, and eye movements) that facilitates backward ambulation in the *moonwalker* mouse (9, 10). Furthermore, TRPC3 expression is increased in mice with contextual fear memory deficits, suggesting a role for TRPC3 in regulating hippocampal neuron excitability associated with memory function (11). In cardiomyocytes and blood vessels, TRPC3 is an essential component of the cellular mechanisms by which vasoconstrictors regulate blood pressure (12, 13). Vasoconstrictors, such as angiotensin II, bind to phospholipase C–coupled receptors, increasing the intracellular levels of DAG, which in turn activates TRPC3 (14). Upon activation, TRPC3 channels induce membrane depolarization and opening of L-type Ca^{2+} channels, increasing intracellular Ca^{2+} and promoting vasoconstriction (15). Likewise, in the cerebellum, TRPC3 activation is downstream of metabotropic glutamate receptors whose activation triggers DAG generation (8). Although DAG is sufficient to activate the channel (14), TRPC3 gating is modulated by additional factors, such as phosphoinositides, glycosylation, phosphorylation, and associated proteins, such as calmodulin and the IP_3 receptor (16). Despite its relevance in the nervous and vascular systems, the TRPC3 gating mechanism remains elusive. Selective compounds for individual TRPC channels are sparse (17, 18); hence, it is expected that structural and mechanistic information will facilitate rational drug design, the outcome of which could sharpen the pharmacological tools and development of new strategies to control neurological disorders and blood pressure.

The structures of TRP channels are being extensively investigated using cryo-EM (19). Recently, a huge step in structural information has been achieved for the subfamily of TRPC channels with the determination of the cryo-EM structures of TRPC4 (20, 21), the full-length (22) and cytoplasmic domain (CPD) of TRPC6 (23), and TRPC3 (22, 24). The TRPC3 structure from Tang *et al.* (22) was obtained using nanodiscs in a closed state despite the presence of the DAG analog, 1-oleoyl-2-acetyl-*sn*-glycerol. The TRPC3 structure from Fan *et al.* (24) was obtained in detergent (digitonin) also in a closed state. Although these structures shared overall topology, they diverge in the CPD spatial organization. Whether these differences are introduced by preparation methods or represent conformational variations that reflect physiologically relevant states remains to be determined.

A TRPC subunit consists of an N terminus formed by four ankyrin repeats, the linker helical domain (LHD; linker helices 1–9), and the pre-S1 elbow. The N terminus is followed by six membrane-spanning helices (S1–S6) and a pore helix connecting to a re-entrant loop that forms the selectivity filter. The TRP helix is immediately adjacent to S6, and the C terminus consists of two α-helices connected by a small linker. Although there are differences in the transmembrane helices that may relate to differences in gating mechanisms among members, the major architectural diversity in the TRP family is their CPDs (23, 25–29). The observed structural diversity suggests that the CPD confers subtype-specific function to the receptor, such as serving as an interface for protein interactions and allosteric gating modulation. For instance, the TRPC3 CPD acts as a biological sensor by decoding physiological cues in the intracellular environment to regulate channel function. Importantly, the C terminus contains a calmodulin (CaM)/IP_3 receptor–binding site (CIRB) (30); the Ca^{2+}–CaM complex binds to the CIRB and inhibits TRPC3 channel activity, whereas at low Ca^{2+} concentrations, the IP_3 receptor competes for CIRB and enhances channel activation (31). Moreover, enhanced activity is also observed in an alternatively spliced variant of mouse TRPC3, which lacks the N-terminal half of the CIRB (32). Collectively, the CPDs have been functionally identified as a locus that modulates TRPC channel gating.

Combining structural and functional approaches, our data show that the TRPC3 CPD is a stable module involved in channel assembly and allosteric gating. This domain is made of ankyrin repeats pierced radially by four horizontal helices (HHs) that converge and transition into a coiled-coil bundle. Notably, the CPD structure reveals a domain swap in the center of the tetrameric assembly, highlighting a unique fold for the TRPC subfamily. Functional characterization of mutants demonstrates that TRPC3 activity increases by shortening the length of the connecting loop between the TRP and horizontal helices; conversely, elongating the length of the loop has the opposite effect. Hence, our results support that the C-terminal loop fine-tunes the allosteric coupling between the cytoplasmic and transmembrane domains.

Results

Determination of the human TRPC3 structure

To determine the structure of TRPC3, we used the full-length human isoform b with a maltose binding protein (MBP) tag at the N terminus. This construct was expressed in Sf9 cells by infecting them with a recombinant baculovirus. Initially, TRPC3 was solubilized in digitonin and further purified using the synthetic digitonin GDN (the sample referred to as $TRPC3_{GDN}$ hereafter). In the final purification step, TRPC3 migrated as a stable and pure monodisperse species as determined by size-exclusion chromatography, SDS-PAGE (Fig. 1*A*), and negative-stain EM (data not shown). Two-dimensional (2D) class averages of $TRPC3_{GDN}$ particles in vitreous ice revealed elements indicative of α-helices in the tetrameric channel (Fig. 1*B*). We were able to calculate a 3D map by collecting a large data set and using a subset of particles that produced class averages showing well-defined membrane-spanning α-helices in the micelle (Fig. S1*A* and Table 1). The final EM density map had an overall resolution of 5.8 Å (Fig. S1, *C* and *D*). At this resolution, the secondary structures forming the transmembrane domain (TMD) and the CPD are clearly resolved (Fig. 1*C*). The TMD was surrounded by signals from the detergent micelle (Fig. 1, *C* and *D*) that disappeared when the map was viewed using a density threshold that optimally resolves the membrane-spanning α-helices. The channel pore opens into a large chamber inside the CPD located below the TMD (Figs. 1*E* and S6*C*). The ions that pass through the channel will enter this chamber and subsequently exit through openings between the LHD and TMD or fenestrations between the ankyrin repeats (Fig. 1*E*). Overall, $TRPC3_{GDN}$ displays a com-

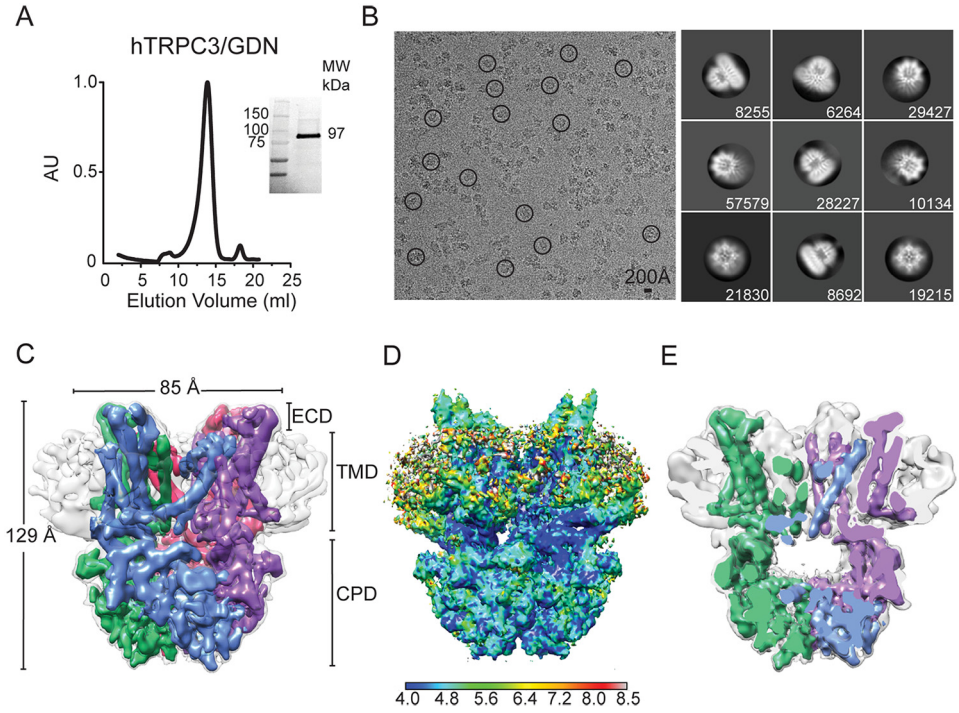

Figure 1. Cryo-EM structure of full-length human TRPC3 at 5.8 Å. *A*, size-exclusion chromatography profile of digitonin-solubilized and GDN-purified TRPC3 from Sf9 cells. *Inset*, stain-free protein on SDS-PAGE gel corresponds to TRPC3 monomer (97 kDa). *B*, *left*, micrograph after motion correction of TRPC3 in GDN micelles ($TRPC3_{GDN}$), taken on an FEI Polara microscope. Note that particles are monodisperse and some are *circled* in *black*. *Right*, representative 2D class averages of $TRPC3_{GDN}$. Particles were aligned and classified in RELION 2.1. The number of particles in each class is shown in the *lower right corner* of each *box*. *C*, electron density map of $TRPC3_{GDN}$ tetrameric assembly. GDN micelle is denoted in *light gray* at a higher threshold than the four subunits, colored in *blue*, *green*, *pink*, and *purple*. *D*, side view of $TRPC3_{GDN}$ with local resolution calculated in ResMap indicated by the heat map scale bar. High- to low-resolution runs as *blue* to *red*, from 4.0 to 8.0 Å. *E*, side view cross-section of the tetrameric $TRPC3_{GDN}$ highlighting the hollow inner chamber below the transmembrane domain. *AU*, arbitrary units; *ECD*, extracellular domain.

Table 1

Data collection and model refinement statistics for $TRPC3_{PMAL}$ and $TRPC3_{GDN}$

Microscope and image processing information for both $TRPC3_{PMAL}$ and $TRPC3_{GDN}$ data collection and refinement statistics for the final models of the TRPC3 CPD and full-length TRPC3 models are shown. Alanine model refers to the full-length polyalanine model of TRPC3. Hybrid model refers to the poly-alanine model TMD with the cytoplasmic domain built using molecular replacement of the TRPC6 CPD (PDB code 6CV9) and refinement in $TRPC3_{GDN}$. All validation and statistics were calculated using MolProbity. RMSD, root mean squared deviation. Values to left of parentheses indicate Total particle count, and values inside parentheses indicate particles in 2D averages.

Data collection and processing	**$TRPC3_{GDN}$ Polara**	**$TRPC3_{GDN}$**		**$TRPC3_{PMAL}$ Titan Krios**
Nominal magnification	31000x			105000x
Voltage (kV)	300			300
Electron exposure ($e^-/Å^2$)	100			48.9
Defocus range (μm)	-2.0 - -5.0			-1.2 - -3.0
Pixel size (Å)	1.247			1.096
Symmetry group	C4			C4
No. of micrographs	3283			2032
Total particle count	1,023,730 (576,237)			464,991 (149,602)
Particles in final reconstruction	38,656			19,526
Map resolution (Å)	5.8			4.0
Map sharpening B factor ($Å^2$)	-179			-126
Refinement	**Alanine model**	**Hybrid model**		**Full atom model**
		Full model	**CPD only**	
Model resolution range (Å)	319.229-5.80	319.229-5.80	319.229-5.80	280.57-4.37
No. of residues (monomer)	490	490	215	288
No. of atoms (monomer)	2450	3222	1677	2293
No. of bonds (monomer)	2439	3237	2100	2322
B factors ($Å^2$)	375.04-41.50	436-01-79.20	324.38-79.20	191.00-67.19
Mean	201.00	219.69	207.38	130.77
RMSD				
Bond lengths (Å)	0.005	0.006	0.006	0.005
Bond angles (°)	0.942	1.142	1.274	1.137
Validation				
MolProbity score	1.67	1.83	2.02	1.70
Clashscore	4.35	6.92	8.96	4.18
Rotamer outliers	0.00%	0.00%	0.00%	0.00%
C-beta outliers	0	0	0	0
Ramachandran plot				
Favored	92.74%	93.11%	90.14%	91.49%
Allowed	7.26%	6.89%	9.96%	8.51%
Disallowed	0.00%	0.00%	0.00%	0.00%

pact two-tiered architecture when compared with the transient receptor potential melastatin 4 (TRPM4; a channel with similar fold) (27, 33, 34), 129 *versus* >150 Å, respectively.

The structure of the TRPC3 cytoplasmic domain

In a recent study, we solved the structure of the *Mus musculus* TRPC6 channel CPD reconstituted in PMAL-C8 at 3.8-Å resolution (23). In those biochemical conditions, the TRPC6 TMD was flexible and appeared as a diffuse density in the cryo-EM class averages. Conversely, the TRPC6 CPD was well-structured, and by masking out the TMD in the 3D classification using RELION (35, 36), we were able to determine the structure of the CPD. We followed the same approach in an attempt to increase the resolution of the TRPC3 CPD. In this preparation, full-length TRPC3 was solubilized in DDM, purified, and reconstituted into PMAL-C8 (referred to as $TRPC3_{PMAL}$ hereafter). $TRPC3_{PMAL}$ migrates as a stable and pure monodisperse species as determined by size-exclusion chromatography and SDS-PAGE (Fig. 2*A*). The particles of $TRPC3_{PMAL}$ were monodisperse in vitreous ice, and their 2D class averages displayed features corresponding to α-helices in the CPD (Fig. 2*B*). The $TRPC3_{PMAL}$ TMD was flexible and diffuse in the cryo-EM class averages (Fig. 2*B*, *white arrows*) when compared with $TRPC3_{GDN}$ (Fig. 1*B*). We were able to calculate an EM density map of the $TRPC3_{PMAL}$ CPD at an average resolution of 4.0 Å (Figs. 2*C* and S2, *A–C*). The EM density map lacked any characteristic TMD α-helices (Fig. 2*D*). As expected,

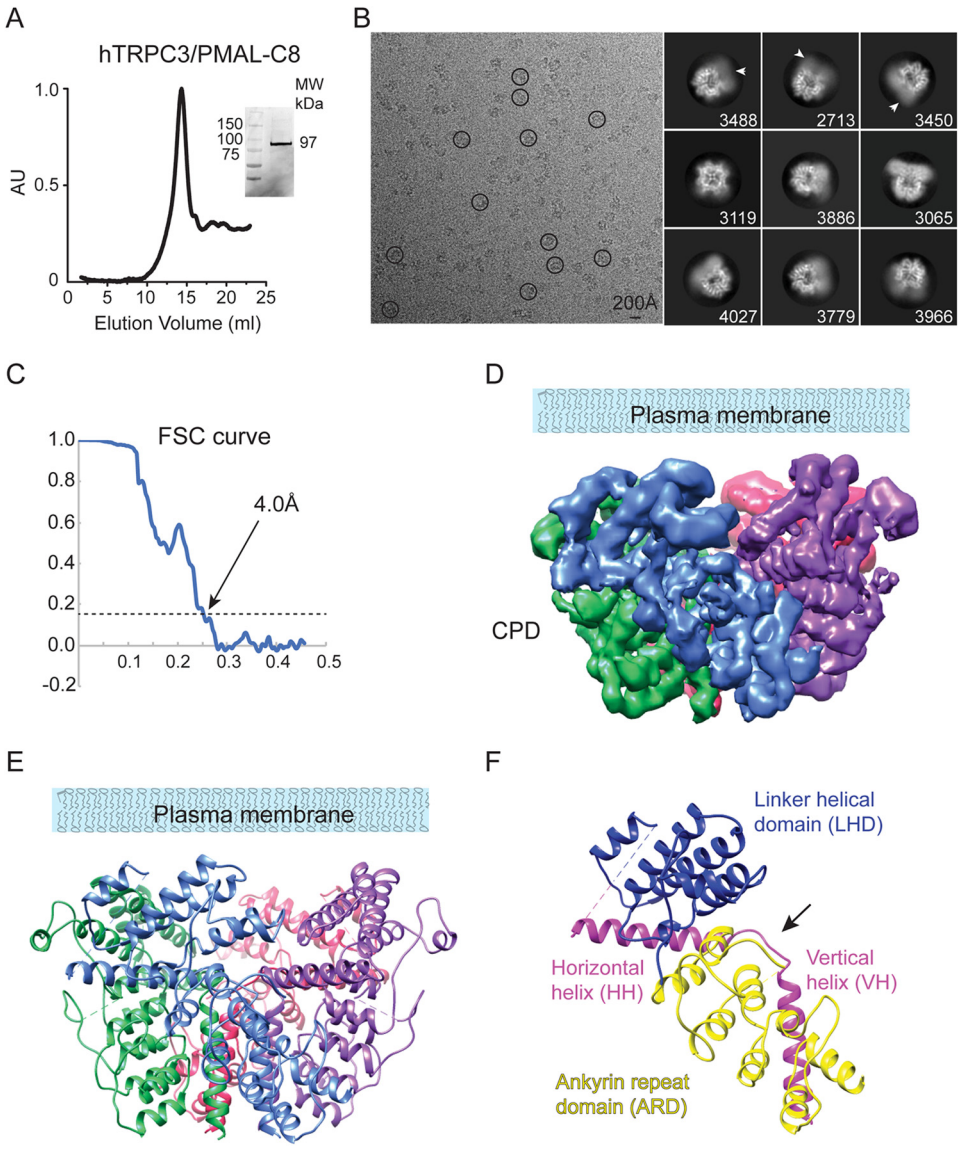

Figure 2. Cryo-EM structure of the TRPC3 CPD at 4.0 Å. *A*, size-exclusion chromatography profile of PMAL-C8–stabilized TRPC3 protein. *Inset*, stain-free protein on the SDS-PAGE gel corresponds to the size of the purified channel monomers (97 kDa). *B*, *left*, micrograph after motion correction of TRPC3 in PMAL-C8 ($TRPC3_{PMAL}$), taken on a Titan Krios. Note that particles are monodisperse and some are *circled* in *black*. *Right*, representative 2D class averages of $TRPC3_{PMAL}$. Particles were aligned and classified in RELION 2.1, and the number of particles in each class is shown in the *lower right corner* of each *box*. *Arrows* indicate the diffuse density of the TMD. *C*, FSC curve showing a 4.0-Å cutoff at the gold standard value of 0.143. *D*, electron density map of TRPC3 CPD tetrameric assembly. *E*, ribbon diagram of the atomic model generated from the EM density map shown in *D*. *F*, CPD ribbon diagram of a single $TRPC3_{PMAL}$ subunit. The subdomains are labeled as ARD (*yellow*), LHD (*blue*), and the C-terminal HH and VH (*pink*). The *black arrow* highlights the linker between the HH and VH. *AU*, arbitrary units.

the CPD displayed lower resolution at its junction to the flexible TMD (Fig. S2*D*).

The cryo-EM density map is of sufficient quality to build an atomic model of the CPD *de novo* (Fig. 2, *D* and *E*, and Table 1). The CPD model was built from residues Thr^{37}–Glu^{295} for the N terminus and Thr^{773}–Leu^{819} for the C terminus. Our model is in agreement with the predicted topology of TRPC3's primary structure (Fig. S3), allowed us to resolve individual polypeptides as well as large side chains (Fig. S4), and resembles the CPD structure of the full-length channel obtained in nanodiscs (22); hence, we consider our structure to be physiologically relevant. The N- and C-terminal segments assemble into a stable tetramer whose global architecture resembles a bowl (Fig. 2, *D* and *E*). The N terminus contains four ankyrin repeats (AR1–4) followed by the LHD composed of α-helices (LH1–8). In the C terminus, the HH makes a 100° downward turn and transitions into the vertical helix (VH) through a short linker (Fig. 2*F*, *black arrow*). The $TRPC3_{PMAL}$ CPD arrangement is comparable with those observed in TRPA1 (26), TRPM4 (27, 33, 34), and TRPM8 (29) in which the N-terminal domain and the C-terminal coiled coil engage in multiple interactions and contribute to the tetrameric assembly of the channel. Notably, the $TRPC3_{PMAL}$ CPD surface potential exhibits a striped distribution as the negative charges in the upper and lower part of the bowl surround a patch of neutral and positive charges (Fig. S5*A*).

In the TRPC6 CPD, the lower half of the domain exhibits an overall negative charge, and the upper half is mainly neutral and positive (23) (Fig. S5*E*). These different surface potential distributions might be relevant for determining the specificity of interaction between the CPD and intracellular components.

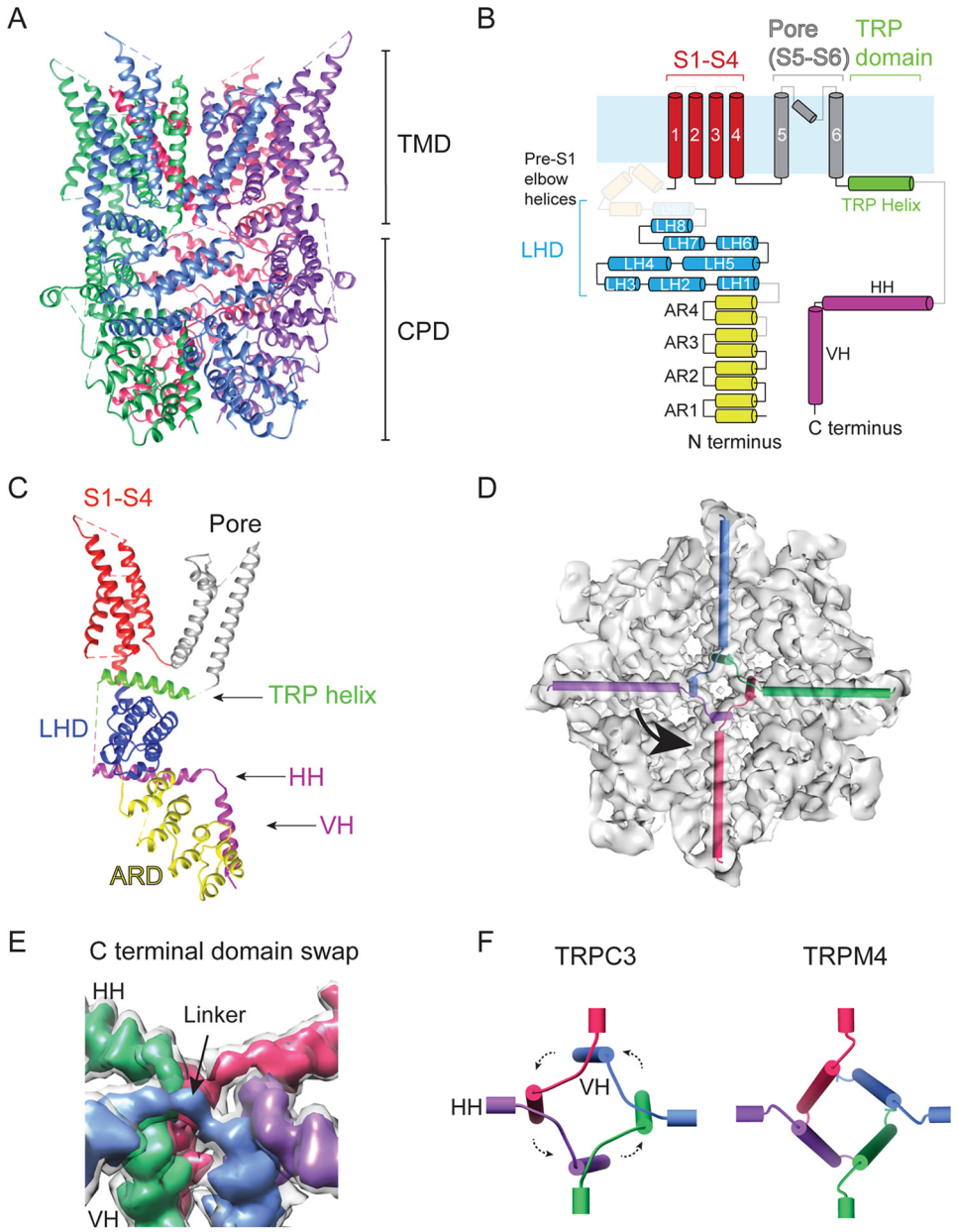

Figure 3. Detailed structural features of TRPC3. *A*, ribbon diagram of the TRPC3 model built from the EM density map shown in Figs. 1*C* and 2*D* with the four subunits in *blue*, *green*, *pink*, and *purple*. *B*, cartoon representation of the secondary structure organization of a single TRPC3 subunit. ARD is in *yellow*, LHD is in *blue*, transmembrane helices are in *red* (S1–S4) and *gray* (S5, pore helix, and S6), the TRP domain helix is in *green*, and the C-terminal helices are in *pink*. *Light blue* represents the plasma membrane. Regions not resolved in the structure are *shaded* out. *C*, the ribbon diagram structure of a single TRPC3 subunit. The domains are color-coded in the same way as in *B*. *D*, top view of TRPC3 with HHs and VHs represented by *cylinders* inside the electron density map, highlighting the C-terminal helices' domain swaps. *E*, close-up look at the domain swap that occurs at the intersection of the HHs and VHs. The map is displayed at two threshold levels with the four-subunit map in *light gray* and four different subunits in colors showing the connection between the HHs and VHs. *F*, cylindrical representation of the intersection of the four HHs and VHs of TRPC3 (*left*) and TRPM4 (*right*; PDB code 6BCL). Note the lack of domain swap in TRPM4.

The inner surface of the $TRPC3_{PMAL}$ bowl displays a negative surface potential arising from the HHs (Fig. S5*B*), similar to TRPC6 (Fig. S5*F*). The CPD exhibits four openings, adjacent to the coiled coil formed by four VHs, lined by negative charges (Fig. S5, *C* and *D*, arrows and yellow circles); hence, the CPD might have a direct impact on TRPC3 ionic currents.

Overall architecture of TRPC3

The $TRPC3_{GDN}$ electron density map was first interpreted by constructing a *de novo* polyalanine model (Table 1). Next, a "hybrid" full-length TRPC3 atomic model was generated by combining our polyalanine model (from residues 296–311 and 370–621) of the TMD with a full-atom model of the CPD (Thr^{37}–Glu^{295} and Thr^{773}–Leu^{819}) (Fig. 3 and Table 1). The N terminus connects to the S1 helix of the TMD through the pre-S1 elbow (Figs. 3, *B* and *C*, and S6, *A* and *B*). Loops (*e.g.* between AR3 and AR4) and helices (*e.g.* LH9) that are *shaded* out in Fig. 3*B* were not resolved in our structure but resolved elsewhere (22, 24). Notably, the C-terminal loop connecting the TRP and the HH helices is not resolved in any of the TRPC3 structures. Near the central axis, the ankyrin repeats make contact with the VHs (Fig. S4*A*). The linker helical

domains form a layer proximal to the plasma membrane (Fig. S6*B*) and engage in extensive contact with the HHs (discussed below).

Similar to other six-transmembrane-segment cation channels, the S1–S4 domain is at the periphery of the TMD (Fig. S6), and the re-entrant loop with a pore helix links the S5 and S6, forming the pore (Fig. 3*C*) (37). The TMD polypeptide re-enters the cytoplasm via the TRP helix, which connects to an HH through an unresolved loop. The HHs penetrate the bowl from the side and converge at the center, forming a cross shape when viewed along the central axis (Fig. 3, *D* and *E*). The VH forms a strong contact point with AR1, which we suggest is an anion–π interaction between Asn^{51} and Tyr^{816} (Fig. S7*A*). This contact point is also seen in TRPC6 between Asn^{109} and Tyr^{895} (23). On the periphery of the CPD, our structure also shows extensive intrasubunit interactions. Once such contact is formed between Tyr^{72} in the first loop between AR1 and AR2 and His^{177} in AR4 of the adjacent subunit (Fig. S7*B*). Interactions in both the interior and exterior of the CPD allow it to exist as a stable module even when the TMD is heterogeneous, like in our structure solved in PMAL-C8.

We also see interactions between two adjacent VHs. Most of the side chains in this region are small and not well-resolved, but a point of contact can be seen in the density between Val^{799} and Leu^{804}, which we speculate is a stabilizing hydrophobic interaction (Fig. S7*C*). There are likely other points of interaction between the VH and HHs in this part of the protein, but our resolution is not high enough to describe them. Because the HH is coupled to the TRP helix, which is attached to S6 (channel gate), we suggest that changes in residue contacts on the HH could directly impact channel gating. Indeed, focal segmental glomerulosclerosis–causing mutations that affect channel gating are found in the HH and its associated structures in TRPC6 (23). Notably, the structure of TRPC3 revealed a C-terminal domain swap in the center of the tetrameric assembly (Fig. 3*E*). This arrangement is characterized by a counterclockwise crossover of linkers that connect the HHs and VHs. A similar domain swap is observed in TRPC6 (22, 23). In contrast, this arrangement is absent in other members of the TRP subfamilies, such as TRPM8, TRPA1, and TRPM4 (Fig. 3*F*); hence, the C-terminal domain swap might be a unique fold of the TRPC subfamily.

Conformational diversity in the cytoplasmic domain

Two TRPC3 cryo-EM structures have been solved recently (22, 24). In Fan *et al.* (24), TRPC3 was solved in digitonin, whereas the structure in Tang *et al.* (22) was solved in nanodiscs; hereafter, we will refer to each structure as $TRPC3_{digitonin}$ and $TRPC3_{nanodisc}$, respectively. The structural features of our $TRPC3_{GDN}$ model agree with the $TRPC3_{nanodisc}$ in the TMD as well as in the CPD (Fig. S7*D*). In contrast, we observed major differences in the CPD of $TRPC3_{GDN}$ (our structure) compared with $TRPC3_{digitonin}$. Particularly, we observed differences in the geometric arrangement of the HHs. In $TRPC3_{GDN}$, the angle formed between the HHs in opposite subunits is 172° (Fig. 4*A*), whereas in $TRPC3_{digitonin}$ this angle is 153° (Fig. 4*B*). The angles formed by TRP helices of opposite subunits are similar (~154°); hence, the TRP helix and the HH are maintained nearly parallel to each other in the $TRPC3_{digitonin}$ structure, whereas in our model they are not (Fig. 4, *A–C*, *black dotted lines*). Interestingly, the positions of the TRP helix and HH in $TRPC3_{digitonin}$ are similar to those observed in TRPC4 (20). We have captured a conformational state in which the HHs are nearly parallel to the membrane plane (Fig. 4*C*, *top*); this putative conformation was also observed in the $TRPC3_{nanodisc}$ structure. Conformational changes in the HH could be transduced to the ion channel gate (S6 segment); therefore, the loop connecting the TRP helix and the HH might play a critical role in channel gating.

Interestingly, our structure displays a counterclockwise rotation of AR1–3 when compared with those of $TRPC3_{digitonin}$ (Fig. S7*E*). As a consequence, the ankyrin repeats are closer to each other and to the VH (Fig. 4, *D* and *E*, *double-headed arrows*). These changes reduce the size of the lateral fenestrations between the ankyrin repeat domains (ARDs) and could decrease the movement of ions and small molecules in and out of the cytoplasmic cavity. It is also possible that these ARD displacements will expose distinct sites for interaction with intracellular components. Moreover, we observed that the intersubunit interface of the coiled-coil domain is larger in our structure (14.7 Å) than in the $TRPC3_{digitonin}$ structure (7.8 Å) (Fig. 4, *D* and *E*, *dotted circles*), likely due to the 4.5° difference between the VHs in both structures (Fig. 4*C*, *bottom*). Unlike the structures of $TRPC3_{GDN}$ and $TRPC3_{nanodisc}$, $TRPC3_{digitonin}$ does not display a C-terminal domain swap, resembling the TRPM4 organization (Figs. 4*F*, *bottom panel*, and S7F). The cartoon shown in Fig. 4*G* summarizes the major differences between $TRPC3_{GDN}$ and $TRPC3_{digitonin}$ highlighted with *arrows*.

The C-terminal loop fine-tunes channel function

Based on the TRPC3 structural comparisons, we hypothesize that upward and downward movements of the HH alter TRPC3 gating via the C-terminal loop connecting the TRP helix and HH. Indeed, previous work reported that a rodent alternative splice variant (TRPC3c), in which 18% of the C-terminal loop and the first three amino acid residues of the HH helix are absent, displays enhanced activity when compared with the longest isoform (32). We engineered the equivalent splice variant into the human TRPC3 isoform b (Δ28TRPC3) and found an increase in channel activity in response to the specific agonist GSK-1702934A (GSK-170) when compared with WT as determined using the ratio of current amplitudes produced by 0.2 and 1 μM GSK-170 at a holding potential of +100 mV (Fig. 5, *B*, *C*, and *G*). CaM inhibits TRPC3 function by binding to the CIRB domain (Fig. S8*B*, black arrow) (30), and the Δ28TRPC3 lacks the N-terminal half of the CIRB (Fig. 5*A*). Therefore, this construct would not allow us to determine whether the change in channel function is solely due to the C-terminal loop. To this end, we generated a shorter construct lacking six amino acid residues (Δ6TRPC3) without disrupting the CIRB (Fig. 5*A*). We found that Δ6TRPC3 enhances TRPC3 activity similarly to Δ28TRPC3 (Fig. 5, *D* and *G*). Importantly, we observed in most of our whole-cell recordings that background channel activities (*i.e.* currents without agonist) were higher in the Δ28TRPC3 and Δ6TRPC3 when compared with WT TRPC3 (Fig. S8*A*).

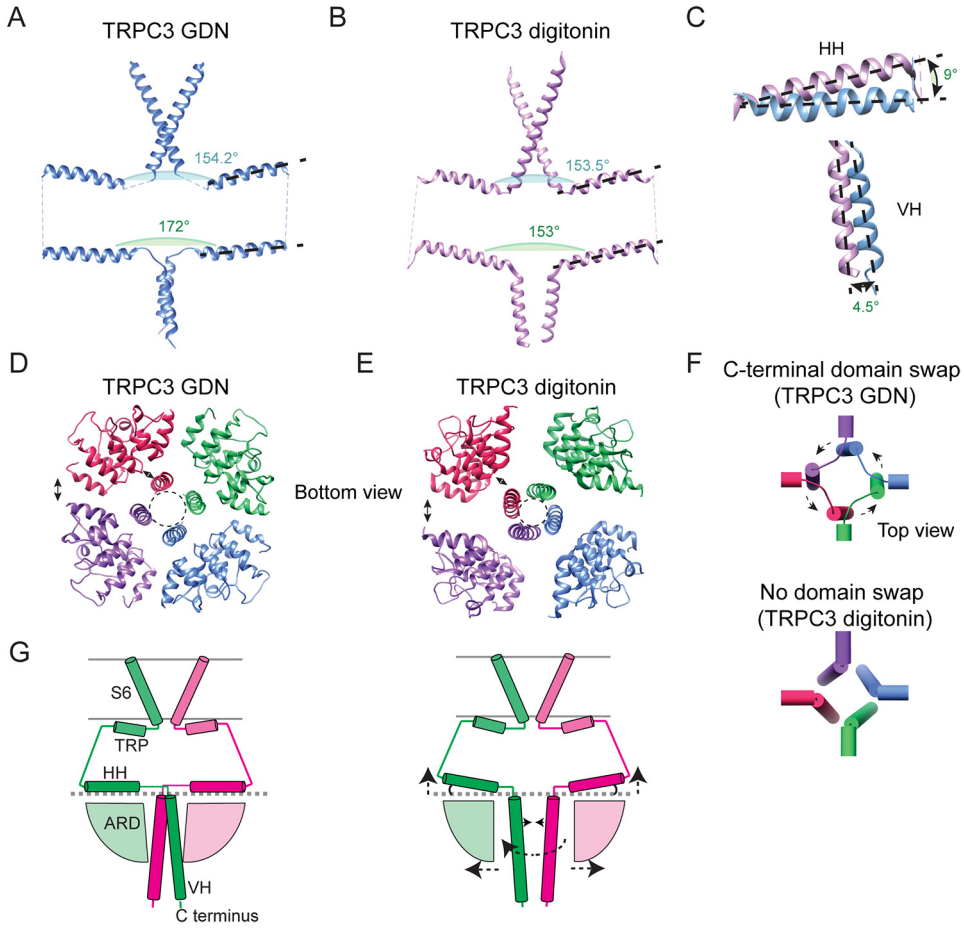

Figure 4. Structural diversity of the CPD. Two opposite subunits of the $TRPC3_{GDN}$ (*A*) and the $TRPC3_{digitonin}$ (PDB code 6CUD) (*B*) structures showing S6 segments, TRP helices, HHs, and VHs. Angles between opposite TRP helices and HHs are indicated. *C*, close-up look comparing the angles of the HH (*top*) and VH (*bottom*) of the $TRPC3_{GDN}$ and $TRPC3_{digitonin}$ structures. *D* and *E*, bottom views of the $TRPC3_{GDN}$ (*D*) and $TRPC3_{digitonin}$ (*E*) structures. Note, that the ARDs in the $TRPC3_{GDN}$ structure are closer to each other at the periphery of the CPD and to the VHs at the central axis, indicated by the *double-headed arrows*. *F*, organization of the HHs and VHs in $TRPC3_{GDN}$ (*top*) and $TRPC3_{digitonin}$ (*bottom*) structures. Note, that the domain swap is absent in $TRPC3_{digitonin}$. *G*, cartoon summarizing the differences observed in the CPDs of the TRPC3 structures.

Conversely, we observed a decrease in channel activity when elongating the C-terminal loop with the addition of four glycines (Fig. 5, *E* and *G*). This result is furthered by the finding that TRPC3 activity was further decreased by elongating the loop and increasing its flexibility with the addition of eight glycines (between Gly^{743} and Asn^{744}) and a neighbor single point mutation (M742G; Fig. 5, *F* and *G*). We also observed that the linker-elongated construct M742G+8G displays lower background currents when compared with WT and Δ28TRPC3 (Fig. S8*A*). Given these results (different deletion or insertion locations yield distinct background currents and channel activation), it is unlikely that we are altering the affinity of the mutant channels for GSK-170 but rather impairing the coupling between the C-terminal domain and the TMD. Our results support the idea that there is a correlation between the length of the linker and the magnitude of channel modulation; specifically shortening the C-terminal loop increases channel activity by creating a stronger coupling between the TRP helix and the HH. It is tempting to speculate that binding of the Ca^{2+}–CaM complex inhibits channel activity by restricting HH movement and decreasing allosteric coupling.

Discussion

Unlike the ionotropic glutamate receptors that transfer information on a millisecond time scale (38), the activation and desensitization of TRPC3-mediated currents are on the order of seconds, often requiring the upstream activation of metabotropic glutamate and muscarinic acetylcholine receptors (8, 39). Given the slower time course of action compared with fast-excitatory synaptic transmission, TRPC3 likely modulates the sensitivity of neurons to fire action potentials (40). Consistent with this idea, pharmacological inhibition of TRPC3 influences simple spike frequency in Purkinje neurons (41). At the behavioral level, a TRPC3 gain-of-function mutation in the *moonwalker* mouse, T573A, results in cerebellar ataxia that facilitates backward ambulation (9). Mechanistic information on TRPC3 channel gating, including how TRPC3 integrates multiple intracellular signals, is critical for understanding its biological roles. Our structural and functional analyses provide insights into the conformational changes that regulate channel function.

Our TRPC3 structures in PMAL-C8 and GDN indicate that the CPD is a stable domain that can maintain its tetrameric

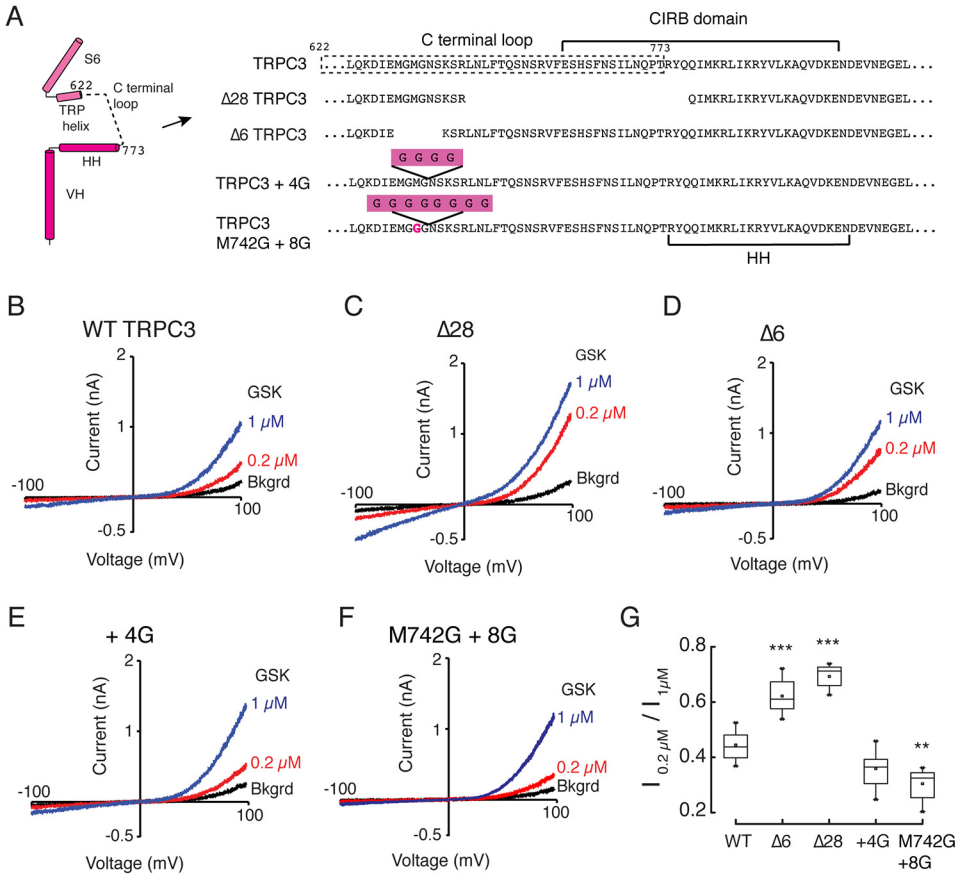

Figure 5. Functional characterization of TRPC3 C-terminal loop mutants. *A*, subunit diagram and amino acid sequence highlighting the changes made in the C-terminal loop of human TRPC3 to generate the deletion constructs Δ749–776 (Δ28TRPC3), Δ740–745 (Δ6TRPC3), and the two glycine insertion constructs TRPC3+4G and M742G+8G. Shown are representative whole-cell recordings from HEK293 cells expressing TRPC3 (*B*), Δ28TRPC3 (*C*), Δ6TRPC3 (*D*), TRPC3+4G (*E*), and M742G+8G (*F*). Currents were evoked by 0.2 (*red*) and 1 μM (*blue*) GSK-170 (*GSK*). *G*, box-plot summary of the ratio between the current evoked by 0.2 μM and the maximal current at 1 μM GSK-170 at +100 mV. For each construct, we measured $n = 12$ independent whole-cell recordings. Box plots show the mean, median, and the 75th to 25th percentiles. Statistics were calculated using a one-way analysis of variance and Bonferroni test. Error bars indicate the 1 and 99th percentiles, ** indicates $p < 0.05$, and *** indicates $p < 0.001$. *Bkgrd*, background.

assembly even in the presence of a flexible TMD; our CPD and full-length TRPC3 structures resemble that of TRPC3 in nanodiscs (Fig. S7*D*) (22, 24). The architecture of the CPD also provides insights into how subunit assembly occurs in TRPC3. The structure of the mature assembly shows that the HH and VH are buried within the ARD and provide stability and anchorage by securing the bowl-shaped CPD. Notably, domain swaps occur when the four HHs merge near the central axis of symmetry, characterized by a crossover of linkers that connect the HHs and VHs. This organization facilitates intra- and intersubunit interactions between residues at the HHs and VHs; this assembly must confer cooperativity among the subunits and provide enhanced stability to this domain. Contacts between the ARD and VH (Fig. S4*A*) are also conserved in TRPC6 (23) and coincide with the locations of human mutations that cause focal segmental glomerulosclerosis (42–46). Because these disease-causing mutations in TRPC6 affect channel gating without making direct contact with the pore domain, this interface is predicted as a site of allosteric modulation for the TRPC subfamily. Moreover, intracellular molecules that alter these interactions might impact channel gating.

We observed substantial differences in the VH and ARD organization when comparing the $TRPC3_{GDN}$ and $TRPC3_{digitonin}$ structures (22, 24) (Fig. 4, *D*, *E*, and *G*). For instance, the intrasubunit distance between AR1 (Pro^{53}) and the end of the VH (Leu^{819}) is 10.1 Å for $TRPC3_{GDN}$ and 14.3 Å for the equivalent positions in $TRPC3_{digitonin}$. Likewise, the intersubunit space between AR1 and AR4 is 18.4 Å for $TRPC3_{GDN}$ and 22.2 Å for $TRPC3_{digitonin}$. Although it is possible that these differences are due to sample preparation methods, we speculate that TRPC3 can interchange between these two states during gating. If this were the case, the CPD would undergo major conformational changes such that the HH and VH could switch or unwind from a domain-swapped arrangement ($TRPC3_{GDN}$ and $TRPC3_{nanodisc}$) to a nonswapped fold ($TRPC3_{digitonin}$) and back. The TRPC3 nonswapped fold architecture is also seen in other TRP channels, such as TRPM4 (27, 33, 34). Future structure and function experiments are required to determine whether these conformational states occur during TRPC3 gating; it would be interesting to investigate whether TRPM4 can also adopt a domain-swapped arrangement.

TRPC3 is a sensor molecule that integrates a variety of intracellular signals, including bioactive lipids and Ca^{2+} gradients (13). For instance, it was recently shown that a single mutation in the S6 segment behind the pore helix reduces activation by

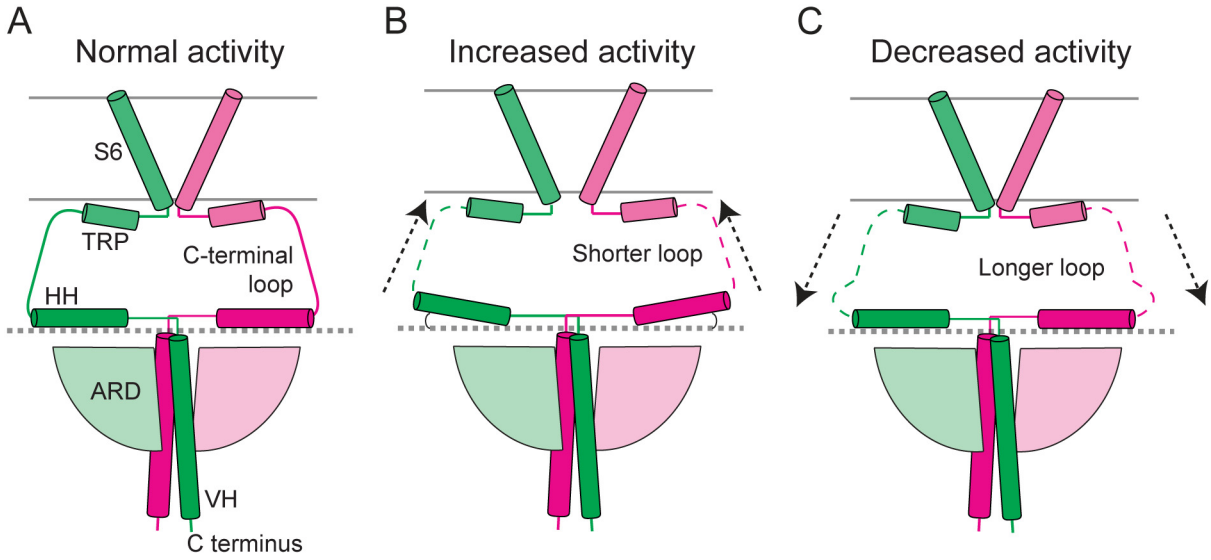

Figure 6. Proposed model for the role of the C-terminal loop in TRPC3 channel function. This diagram summarizes the electrophysiological data in which the C-terminal loop length modulates TRPC3 activity. *A*, schematic of the structure of $TRPC3_{GDN}$. A shorter loop enhances coupling between the HH and the TMD and in turn increases activity (*B*), whereas a longer loop has the opposite effect (*C*).

DAG (47). Phosphorylation after the TRP helix has been shown to negatively regulate channel function (48). The Ca^{2+}–CaM complex inhibits channel activity; however, at low Ca^{2+} concentration, the IP_3 receptor binds the CIRB and enhances its function (31).

How does the cytoplasmic domain modulate channel function? We propose a model in which the HH can bend upward and downward (Fig. 6, *A* and *B*); this rigid-body motion would be transduced to the TRP helix via the connecting loop and in turn influence the channel gate at the S6 segment (Fig. 6). Several lines of evidence, including our own, support this model. First, the TRPC3 structures in GDN and digitonin display different angles of the HH with respect to the membrane, suggesting that the HH can reside in these positions. Second, shortening of the C-terminal loop enhances channel activity, presumably by increasing coupling between the TRP helix and the HH (Fig. 6*B*); hence, the C-terminal loop is a critical region for the allosteric coupling between the cytoplasmic and transmembrane domains. The C-terminal loop might also provide buffering capacity due to its intrinsic flexibility, consistent with the different degrees of bending occurring at the HHs, the decrease in activity when lengthening the loop with glycines (Fig. 6*C*), and the lack of structural organization. Such buffering might be advantageous to prevent spurious modulation caused by fluctuations of the CPD. Third, binding of CaM to the HH inhibits channel opening (31), likely by restricting movement of the HH and decreasing allosteric coupling. It is possible that the mechanism whereby the CPD modulates channel function through the HH and the C-terminal loop is conserved because it has been shown that calmodulin also regulates TRPA1 (49) and TRPM4 (50) function by binding to the corresponding CPD region. Further functional and structural experiments are needed to validate whether the upward movement of the HHs corresponds to a positive modulation of the TRPC3 gating cycle.

Experimental procedures

Cell culture and electrophysiology

Human embryonic kidney 293 (HEK293) cells were cultured in Dulbecco's modified Eagle's medium (Invitrogen) supplemented with 10% fetal bovine serum and 1% penicillin-streptomycin at 37 °C and 5% CO_2. TRPC3 constructs cloned in pMO (a pcDNA3-modified vector) were transfected using Lipofectamine® 2000 (Invitrogen) according to the manufacturer's instructions. Macroscopic currents in the whole-cell patch-clamp configuration were recorded 18–24 h post-transfection. The extracellular solution contained 140 mM NaCl, 2.8 mM KCl, 1 mM $MgCl_2$, 2 mM $CaCl_2$, and 2 mM HEPES, pH 7.4. Pipettes were made of borosilicate glass (outer diameter, 1.5 mm; inner diameter, 1.10 mm; Sutter Instruments) and fire-polished with a resistance between 2.8 and 4.0 megaohms when filled with an intracellular solution that contained 140 mM CsCl, 5 mM EGTA, and 10 mM HEPES, pH 7.2. Currents were recorded with a Multiclamp 700B amplifier (Molecular Devices) using a 1-s ramp from −100 to 100 mV. TRPC3 channel agonist GSK-170 and the antagonist GSK-417651A from Focus Biomolecules were dissolved in DMSO and freshly dissolved in bath solution to the indicated concentration. Data were acquired with a sampling rate of 20 kHz, low-pass filtered (4 kHz), and analyzed offline using Clampfit v10.4.2.0 (Molecular Devices).

Human TRPC3 expression and purification (NP_003296.1)

A DNA construct containing His_8-MBP-hTRPC3b with a conserved single-point mutation, I395V, was cloned into the pFastbac1 expression vector. Recombinant baculovirus was obtained following the manufacturer's protocol (Bac-to-Bac expression system, Invitrogen). Sf9 cells were infected with recombinant baculovirus and harvested by centrifugation 72 h after infection. The cell pellet from 0.8 liter of culture was resuspended and lysed with a high-pressure homogenizer (Avestin) in a hypotonic buffer (36.5 mM sucrose, 50 mM Tris, and 4 mM TCEP,

pH 8) and supplemented with protease inhibitors (1 mM phenylmethanesulfonyl fluoride, 3 mg/ml aprotinin, 3 mg/ml leupeptin, and 1 mg/ml pepstatin). Cell debris was collected by low-speed centrifugation (8,000 × *g* for 15 min at 4 °C). Membranes were collected by ultracentrifugation (100,000 × *g* for 30 min at 4 °C).

TRPC3 in GDN—Membranes were solubilized in Buffer A1 (300 mM NaCl, 4 mM TCEP, and 50 mM Tris, pH 8) supplemented with protease inhibitors. Protein was extracted with 1% digitonin (Millipore) with gentle stirring for 2 h. The detergent-insoluble material was removed by centrifugation (150,000 × *g* for 45 min at 4 °C), and the supernatant was incubated with amylose resin (New England Biolabs) with gentle stirring for 3 h. After loading onto the column and collecting the flow-through, the resin was washed with 10 column volumes of Buffer B1 (300 mM NaCl, 4 mM TCEP, 0.1% digitonin, and 50 mM Tris, pH 8). Afterward, the protein was eluted with Buffer B1 supplemented with 20 mM maltose. The protein then was digested with ProTEV Plus protease (Promega) at 4 °C overnight to remove the MBP tag. Cleaved protein was further purified by size-exclusion chromatography on a Superose 6 10/300 GL column (GE Healthcare) pre-equilibrated with Buffer C1 (200 mM NaCl, 4 mM TCEP, 40 μM GDN, and 50 mM Tris, pH 8). Peak fractions corresponding to the tetrameric channel were collected and concentrated to ~1.2 mg/ml for cryo-EM analysis.

TRPC3 in PMAL-C8—Membranes were solubilized in Buffer A2 (150 mM NaCl, 4 mM TCEP, 10% glycerol, and 50 mM HEPES, pH 7.4) supplemented with protease inhibitors. Protein was extracted with 26 mM DDM (Anatrace) with gentle stirring for 2 h. The detergent-insoluble material was removed by centrifugation (150,000 × *g* for 45 min at 4 °C), and the supernatant was incubated with amylose resin (New England Biolabs) with gentle stirring for 3 h. After loading onto the column and collecting the flow-through, the resin was washed with 10 column volumes of Buffer B2 (150 mM NaCl, 4 mM TCEP, 10% glycerol, 1 mM DDM, 0.1 mg/ml asolectin, and 50 mM HEPES, pH 7.4). Afterward, the protein was eluted with Buffer B2 supplemented with 20 mM maltose. The eluted protein was then mixed with PMAL-C8 (Anatrace) at 1:3 (w/w) with gentle agitation for 2 h at 4 °C. The protein then was digested with ProTEV Plus protease at 4 °C overnight to remove the MBP tag. Cleaved protein was further purified by size-exclusion chromatography on a Superose 6 10/300 GL column pre-equilibrated with Buffer C2 (150 mM NaCl, 4 mM TCEP, and 20 mM HEPES, pH 7.4). Peak fractions corresponding to the tetrameric channel were collected and concentrated to ~0.3 mg/ml for cryo-EM analysis.

Cryo-EM data collection

TRPC3 in GDN—Two microliters (2.0 μl) of 1.2 mg/ml TRPC3 in Buffer C1 were applied to 200-mesh 2/1 C-flat grids that were glow-discharged for 2 min at 25 mA (Quorom K100X). Grids were blotted for 7 s before being plunged into liquid ethane using an FEI MarkIII Vitrobot at 8 °C and 100% humidity. Micrographs were collected in super-resolution mode on a K2 Summit direct electron detector (Gatan) using an FEI Polara F30 microscope operated at 300 kV at the Vanderbilt University cryo-EM facility. Micrographs were collected at a nominal magnification of ×31,000 using a defocus range of −1.8 to −4.8 μm. The images were binned by a factor of 2 during motion correction, resulting in a calibrated pixel size of 1.24699 Å/pix. Images were recorded for 8 s at ~12.5 e^-/pix/s over 40 frames, resulting in a total dose of 85–100 $e^-/Å^2$. Data were collected manually and with automation using SerialEM in low-dose conditions.

TRPC3 in PMAL-C8—Two microliters (2.0 μl) of 0.3 mg/ml TRPC3 in PMAL-C8 amphipol in Buffer C2 were applied to a 400-mesh C-flat holey carbon 2/1 grid that was glow-discharged for 2 min at 25 mA. The grid was blotted for 8 s before being plunged into liquid ethane using an FEI MarkIII Vitrobot at 8 °C and 100% humidity. Micrographs were collected using a FEI Titan Krios microscope equipped with a Cs corrector at Washington University in St. Louis (Center for Cellular Imaging). Images were recorded using a Gatan K2 direct electron detector equipped with an energy filter (Gatan BioQuantum). Images were taken at a nominal magnification of ×105,000 using EPU software–aided automation over 30 h using counting mode on the detector. Under low-dose conditions, the specimen was exposed at ~8 e^-/pixel/s for 7.4 s over 30 frames, accounting for a total dose of ~50 $e^-/Å^2$. The calibrated pixel size of the images was 1.096 Å/pix.

Image processing

TRPC3 in GDN sample—Images were motion-corrected by MotionCor2 (51) with a dose-weighting parameter of 2.5 e^-/Å/frame. The CTF was determined using Gctf (52). The image-processing software Focus (53) was used for on-the-fly assessment of images being collected. Low-image-quality micrographs were discarded. Dose-weighted, motion-corrected micrographs were imported into RELION 2.1, and CTF was determined by Gctf (52). Averages with clearly resolved secondary structure in the TMD were moved into 3D classification. Particle images were aligned and classified in 3D using a cryo-EM structure of TRPC6 as a reference (23). This TRPC6 model contains the transmembrane domain, albeit at low resolution. We also aligned the particles using the low-resolution model of full-length TRPC6 generated by random conical tilt reconstruction from a negative-stain data set, which produced a virtually identical outcome as using the vitrified TRPC6 as an initial model. Because negative-stain class averages of full-length TRPC3 and TRPC6 appear nearly identical, our choice of reference is unlikely to introduce model bias. A mask generated from the TRPC6 cryo-EM structure filtered at 50 Å (threshold, 0.00172 with a 5-pix extension and 5-pix soft edge) was used during this round of classification. 3D classification with C4 symmetry imposed was conducted in three different batches; each batch corresponded to different data collection sessions. As a result, the particles were classified into 14 classes altogether (Fig. S1*A*). The best classes from each batch were combined and added up to 38,656 particles. These were subjected to 3D refinement, postprocessing, and local resolution calculations in RELION 2.1, resulting in a final reconstruction at 5.8 Å. Postprocessing was done by applying a B-factor (−179$Å^2$) that was calculated by RELION 2.1 based on the method of Rosenthal and Henderson (54) and a mask generated from the 3D refinement step filtered to 10 Å (threshold, 0.0085 with a 5-pix extension and 5-pix soft edge) (Fig. S1). Detailed statistics are provided in Table 1.

The resolution of the map was estimated by the gold-standard Fourier shell correlation (FSC) in RELION 2.1 using the FSC = 0.143 criterion.

TRPC3 in PMAL-C8 sample—Images were motion-corrected with a dose-weighting parameter of 1.63 e^{-}/Å/frame using MotionCor2 (51). Dose-weighted, motion-corrected micrographs were imported into RELION 2.1. The CTF was determined by Gctf (52) using a Cs aberration parameter of 0.001, and low-image-quality micrographs were discarded from further analysis. Putative particles were identified by autopicking using representative class averages obtained from manually picked particles as templates. Particles were extracted with a mask size of 160 Å and box size of 256 × 256 pixels, and they underwent 25 iterations of 2D classification. Averages with clearly resolved secondary structure in the CPD were classified in 3D into five classes using a starting model of the TRPC6 CTD (23). A mask generated from the TRPC6 structure filtered at 10 Å (threshold, 0.0205 with a 7-pix extension and 7-pix soft edge) was used during this round of classification. The best two models, which contained 19,398 particles, were subject to 3D refinement, postprocessing, and local resolution calculations in RELION 2.1, resulting in a final reconstruction at 4.0 Å. Postprocessing was done by applying a B-factor ($-126Å^2$) that was calculated by RELION 2.1 based on the method of Rosenthal and Henderson (54) and a mask generated from the 3D refinement step filtered at 10 Å (threshold, 0.0107 with a 4-pix extension and 4-pix soft edge) (Fig. S2). Detailed statistics are provided in Table 1. The resolution of the map was estimated by the gold-standard FSC in RELION 2.1 using the FSC = 0.143 criterion.

Model building refinement and validation

For both structures, secondary structure was manually inserted using Coot. From there, a polyalanine model was first built manually with Coot (Table 1, alanine model) (55). Subsequent amino acid assignment was performed for the CPD by defining the densities of bulky residues in the $TRPC3_{PMAL}$ structure (Fig. S4). A hybrid full-length TRPC3 atomic model was generated by combining our polyalanine model of the TMD with a full-atom model of the CPD. The full-atom models for the tetrameric assemblies were generated using UCSF Chimera (56). All models were optimized using Phenix's real-space refinement tool (57). To prevent overfitting of the models into the density, refinement was run for three cycles with strict geometric restraints of 0.005 for bond length and 0.5 for bond angle while non-crystallographic symmetry (NCS) was imposed. For the $TRPC3_{GDN}$ hybrid model, refinement steps using these parameters were iterated seven times with manual adjustment of the structure to correct for Ramachandran and rotamer outliers and bond angle deviations of more than 4σ. We performed a round of refinement that incorporated morphing, global minimization, secondary structure restraints, simulated annealing, and NCS followed by a round with only morphing. A final two iterations of refinement with strict geometric restraints and manual adjustment in Coot were performed. To conserve helix assignments, secondary structure restraints were used throughout. For the $TRPC3_{PMAL}$ model, refinement steps using these parameters were iterated five times with manual adjustment of the structure to correct for Ramachandran and rotamer outliers and bond angle deviations of more than 4σ. We performed a round of refinement that incorporated morphing, global minimization, secondary structure restraints, simulated annealing, and NCS. A final four iterations of refinement with strict geometric restraints and manual adjustment in Coot were performed. Validations of the final models were performed using MolProbity (58).

Angle measurements

To estimate angles between helices, we created a "pipes and planks" model using UCSF Chimera (56). After exporting an image in the desired position, we used Fiji to obtain the angle values by placing manually three points along the pair of helices. Angles were confirmed in Coot with an error of ±1°.

Visualization

Density maps were displayed using UCSF Chimera (56). The map thresholds in Fig. 1 are 0.0237 for the *transparent gray* map and 0.0239 for the four separately *colored* chains. In Fig. 2, the map threshold for the four *colored* chains is 0.0403.

Data deposits

The EM density map and atomic coordinates for $TRPC3_{PMAL}$ were deposited to the Protein Data Bank (PDB) and EMDataBank (EMDB) under the accession codes 6D7L and EMD-7823. The EM density map and atomic coordinates for $TRPC3_{GDN}$ were deposited to the PDB and EMDB under accession codes 6DJR (polyalanine), 6DJS (hybrid), and EMD-7940.

Author contributions—F. S.-V., C. M. A., T. N., and J. F. C.-M. data curation; F. S.-V., C. M. A., L. O. R., T. N., and J. F. C.-M. formal analysis; F. S.-V., C. M. A., and L. O. R. investigation; F. S.-V., C. M. A., T. N., and J. F. C.-M. writing-review and editing; T. N. and J. F. C.-M. conceptualization; T. N. and J. F. C.-M. resources; T. N. and J. F. C.-M. supervision; T. N. and J. F. C.-M. funding acquisition; T. N. and J. F. C.-M. writing-original draft; T. N. and J. F. C.-M. project administration; J. F. C.-M. methodology.

Acknowledgments—We thank Dr. Valeria Vásquez for experimental advice and critically reading the manuscript, Dr. Efren Maldonado and Dr. Erkan Karakas for advice during model construction, Dr. Alejandro Mata for TRPC3 patch-clamp recordings, Dr. Silvio Panettieri and Dr. George John for synthesis of GSK-1702934A, Dr. Jonathan Jaggar for providing the hTRPC3 clone, and members of the Cordero-Vásquez laboratory for technical assistance. EM data collections using FEI Polara and FEI TF20 were conducted at the Center for Structural Biology's Molecular Cryo-EM facility at Vanderbilt University. We thank Dr. Scott Collier and Dr. Elad Binshtein for support at the facility. We thank Dr. James Fitzpatrick and Michael Rau for providing access and facilitating data collection using the Titan Krios at the Washington University School of Medicine in St. Louis. This work was conducted in part using the central processing unit (CPU) and graphical processing unit (GPU) resources of the Advanced Computing Center for Research and Education (ACCRE) at Vanderbilt University. We used the Distributed Online Research Storage (DORS) storage system supported by National Institutes of Health Grant S10RR031634 (to Jarrod Smith). We acknowledge the use of SBGrid-supported software (59).

References

1. Inoue, R., Jensen, L. J., Shi, J., Morita, H., Nishida, M., Honda, A., and Ito, Y. (2006) Transient receptor potential channels in cardiovascular function and disease. *Circ. Res.* **99,** 119–131 CrossRef Medline
2. Ramsey, I. S., Delling, M., and Clapham, D. E. (2006) An introduction to TRP channels. *Annu. Rev. Physiol.* **68,** 619–647 CrossRef Medline
3. Nilius, B., and Owsianik, G. (2010) Transient receptor potential channelopathies. *Pflugers Arch.* **460,** 437–450 CrossRef Medline
4. Bröker-Lai, J., Kollewe, A., Schindeldecker, B., Pohle, J., Nguyen Chi, V., Mathar, I., Guzman, R., Schwarz, Y., Lai, A., Weißgerber, P., Schwegler, H., Dietrich, A., Both, M., Sprengel, R., Draguhn, A., *et al.* (2017) Heteromeric channels formed by TRPC1, TRPC4 and TRPC5 define hippocampal synaptic transmission and working memory. *EMBO J.* **36,** 2770–2789 CrossRef Medline
5. Hofmann, T., Schaefer, M., Schultz, G., and Gudermann, T. (2002) Subunit composition of mammalian transient receptor potential channels in living cells. *Proc. Natl. Acad. Sci. U.S.A.* **99,** 7461–7466 CrossRef Medline
6. Álvarez-Miguel, I., Cidad, P., Pérez-García, M. T., and López-López, J. R. (2017) Differences in TRPC3 and TRPC6 channels assembly in mesenteric vascular smooth muscle cells in essential hypertension. *J. Physiol.* **595,** 1497–1513 CrossRef Medline
7. Sekerková, G., Kim, J. A., Nigro, M. J., Becker, E. B., Hartmann, J., Birnbaumer, L., Mugnaini, E., and Martina, M. (2013) Early onset of ataxia in moonwalker mice is accompanied by complete ablation of type II unipolar brush cells and Purkinje cell dysfunction. *J. Neurosci.* **33,** 19689–19694 CrossRef Medline
8. Hartmann, J., Dragicevic, E., Adelsberger, H., Henning, H. A., Sumser, M., Abramowitz, J., Blum, R., Dietrich, A., Freichel, M., Flockerzi, V., Birnbaumer, L., and Konnerth, A. (2008) TRPC3 channels are required for synaptic transmission and motor coordination. *Neuron* **59,** 392–398 CrossRef Medline
9. Becker, E. B., Oliver, P. L., Glitsch, M. D., Banks, G. T., Achilli, F., Hardy, A., Nolan, P. M., Fisher, E. M., and Davies, K. E. (2009) A point mutation in TRPC3 causes abnormal Purkinje cell development and cerebellar ataxia in moonwalker mice. *Proc. Natl. Acad. Sci. U.S.A.* **106,** 6706–6711 CrossRef Medline
10. Fogel, B. L., Hanson, S. M., and Becker, E. B. (2015) Do mutations in the murine ataxia gene TRPC3 cause cerebellar ataxia in humans? *Mov. Disord.* **30,** 284–286 CrossRef Medline
11. Neuner, S. M., Wilmott, L. A., Hope, K. A., Hoffmann, B., Chong, J. A., Abramowitz, J., Birnbaumer, L., O'Connell, K. M., Tryba, A. K., Greene, A. S., Savio Chan, C., and Kaczorowski, C. C. (2015) TRPC3 channels critically regulate hippocampal excitability and contextual fear memory. *Behav. Brain Res.* **281,** 69–77 CrossRef Medline
12. Di, A., and Malik, A. B. (2010) TRP channels and the control of vascular function. *Curr. Opin. Pharmacol.* **10,** 127–132 CrossRef Medline
13. Lichtenegger, M., and Groschner, K. (2014) TRPC3: a multifunctional signaling molecule. *Handb. Exp. Pharmacol.* **222,** 67–84 CrossRef Medline
14. Hofmann, T., Obukhov, A. G., Schaefer, M., Harteneck, C., Gudermann, T., and Schultz, G. (1999) Direct activation of human TRPC6 and TRPC3 channels by diacylglycerol. *Nature* **397,** 259–263 CrossRef Medline
15. Xi, Q., Adebiyi, A., Zhao, G., Chapman, K. E., Waters, C. M., Hassid, A., and Jaggar, J. H. (2008) IP3 constricts cerebral arteries via IP3 receptor-mediated TRPC3 channel activation and independently of sarcoplasmic reticulum Ca^{2+} release. *Circ. Res.* **102,** 1118–1126 CrossRef Medline
16. Minke, B. (2006) TRP channels and Ca^{2+} signaling. *Cell Calcium* **40,** 261–275 CrossRef Medline
17. Schleifer, H., Doleschal, B., Lichtenegger, M., Oppenrieder, R., Derler, I., Frischauf, I., Glasnov, T. N., Kappe, C. O., Romanin, C., and Groschner, K. (2012) Novel pyrazole compounds for pharmacological discrimination between receptor-operated and store-operated Ca^{2+} entry pathways. *Br. J. Pharmacol.* **167,** 1712–1722 CrossRef Medline
18. Kiyonaka, S., Kato, K., Nishida, M., Mio, K., Numaga, T., Sawaguchi, Y., Yoshida, T., Wakamori, M., Mori, E., Numata, T., Ishii, M., Takemoto, H., Ojida, A., Watanabe, K., Uemura, A., *et al.* (2009) Selective and direct inhibition of TRPC3 channels underlies biological activities of a pyrazole compound. *Proc. Natl. Acad. Sci. U.S.A.* **106,** 5400–5405 CrossRef Medline
19. Madej, M. G., and Ziegler, C. M. (2018) Dawning of a new era in TRP channel structural biology by cryo-electron microscopy. *Pflugers Arch.* **470,** 213–225 CrossRef Medline
20. Vinayagam, D., Mager, T., Apelbaum, A., Bothe, A., Merino, F., Hofnagel, O., Gatsogiannis, C., and Raunser, S. (2018) Electron cryo-microscopy structure of the canonical TRPC4 ion channel. *Elife* **7,** e36615 CrossRef Medline
21. Duan, J., Li, J., Bo, Z., Chen, G.-L., Peng, X., Zhang, Y., Wang, J., Clapham, D. E., Li, Z., and Zhang, J. (2018) Structure of the mouse TRPC4 ion channel. *bioRxiv* CrossRef
22. Tang, Q., Guo, W., Zheng, L., Wu, J. X., Liu, M., Zhou, X., Zhang, X., and Chen, L. (2018) Structure of the receptor-activated human TRPC6 and TRPC3 ion channels. *Cell Res.* **28,** 746–755 CrossRef Medline
23. Azumaya, C. M., Sierra-Valdez, F., Cordero-Morales, J. F., and Nakagawa, T. (2018) Cryo-EM structure of the cytoplasmic domain of murine transient receptor potential cation channel subfamily C member 6 (TRPC6). *J. Biol. Chem.* **293,** 10381–10391 CrossRef Medline
24. Fan, C., Choi, W., Sun, W., Du, J., and Lu, W. (2018) Structure of the human lipid-gated cation channel TRPC3. *Elife* **7,** e36852 CrossRef Medline
25. Liao, M., Cao, E., Julius, D., and Cheng, Y. (2013) Structure of the TRPV1 ion channel determined by electron cryo-microscopy. *Nature* **504,** 107–112 CrossRef Medline
26. Paulsen, C. E., Armache, J. P., Gao, Y., Cheng, Y., and Julius, D. (2015) Structure of the TRPA1 ion channel suggests regulatory mechanisms. *Nature* **520,** 511–517 CrossRef Medline
27. Autzen, H. E., Myasnikov, A. G., Campbell, M. G., Asarnow, D., Julius, D., and Cheng, Y. (2018) Structure of the human TRPM4 ion channel in a lipid nanodisc. *Science* **359,** 228–232 CrossRef Medline
28. Jin, P., Bulkley, D., Guo, Y., Zhang, W., Guo, Z., Huynh, W., Wu, S., Meltzer, S., Cheng, T., Jan, L. Y., Jan, Y. N., and Cheng, Y. (2017) Electron cryo-microscopy structure of the mechanotransduction channel NOMPC. *Nature* **547,** 118–122 CrossRef Medline
29. Yin, Y., Wu, M., Zubcevic, L., Borschel, W. F., Lander, G. C., and Lee, S. Y. (2018) Structure of the cold- and menthol-sensing ion channel TRPM8. *Science* **359,** 237–241 CrossRef Medline
30. Tang, J., Lin, Y., Zhang, Z., Tikunova, S., Birnbaumer, L., and Zhu, M. X. (2001) Identification of common binding sites for calmodulin and inositol 1,4,5-trisphosphate receptors on the carboxyl termini of Trp channels. *J. Biol. Chem.* **276,** 21303–21310 CrossRef Medline
31. Zhang, Z., Tang, J., Tikunova, S., Johnson, J. D., Chen, Z., Qin, N., Dietrich, A., Stefani, E., Birnbaumer, L., and Zhu, M. X. (2001) Activation of Trp3 by inositol 1,4,5-trisphosphate receptors through displacement of inhibitory calmodulin from a common binding domain. *Proc. Natl. Acad. Sci. U.S.A.* **98,** 3168–3173 CrossRef Medline
32. Kim, Y., Wong, A. C., Power, J. M., Tadros, S. F., Klugmann, M., Moorhouse, A. J., Bertrand, P. P., and Housley, G. D. (2012) Alternative splicing of the TRPC3 ion channel calmodulin/IP3 receptor-binding domain in the hindbrain enhances cation flux. *J. Neurosci.* **32,** 11414–11423 CrossRef Medline
33. Guo, J., She, J., Zeng, W., Chen, Q., Bai, X. C., and Jiang, Y. (2017) Structures of the calcium-activated, non-selective cation channel TRPM4. *Nature* **552,** 205–209CrossRef Medline
34. Winkler, P. A., Huang, Y., Sun, W., Du, J., and Lü, W. (2017) Electron cryo-microscopy structure of a human TRPM4 channel. *Nature* **552,** 200–204 CrossRef Medline
35. Kimanius, D., Forsberg, B. O., Scheres, S. H., and Lindahl, E. (2016) Accelerated cryo-EM structure determination with parallelisation using GPUs in RELION-2. *Elife* **5,** e18722 CrossRef Medline
36. Scheres, S. H. (2012) RELION: implementation of a Bayesian approach to cryo-EM structure determination. *J. Struct. Biol.* **180,** 519–530 CrossRef Medline
37. Long, S. B., Campbell, E. B., and Mackinnon, R. (2005) Crystal structure of a mammalian voltage-dependent Shaker family K^+ channel. *Science* **309,** 897–903 CrossRef Medline

38. Greger, I. H., Watson, J. F., and Cull-Candy, S. G. (2017) Structural and functional architecture of AMPA-type glutamate receptors and their auxiliary proteins. *Neuron* **94,** 713–730 CrossRef Medline
39. Berg, A. P., Sen, N., and Bayliss, D. A. (2007) TrpC3/C7 and Slo2.1 are molecular targets for metabotropic glutamate receptor signaling in rat striatal cholinergic interneurons. *J. Neurosci.* **27,** 8845–8856 CrossRef Medline
40. Zhou, F. W., Matta, S. G., and Zhou, F. M. (2008) Constitutively active TRPC3 channels regulate basal ganglia output neurons. *J. Neurosci.* **28,** 473–482 CrossRef Medline
41. Zhou, H., Lin, Z., Voges, K., Ju, C., Gao, Z., Bosman, L. W., Ruigrok, T. J., Hoebeek, F. E., De Zeeuw, C. I., and Schonewille, M. (2014) Cerebellar modules operate at different frequencies. *Elife* **3,** e02536 CrossRef Medline
42. Winn, M. P., Conlon, P. J., Lynn, K. L., Farrington, M. K., Creazzo, T., Hawkins, A. F., Daskalakis, N., Kwan, S. Y., Ebersviller, S., Burchette, J. L., Pericak-Vance, M. A., Howell, D. N., Vance, J. M., and Rosenberg, P. B. (2005) A mutation in the TRPC6 cation channel causes familial focal segmental glomerulosclerosis. *Science* **308,** 1801–1804 CrossRef Medline
43. Reiser, J., Polu, K. R., Möller, C. C., Kenlan, P., Altintas, M. M., Wei, C., Faul, C., Herbert, S., Villegas, I., Avila-Casado, C., McGee, M., Sugimoto, H., Brown, D., Kalluri, R., Mundel, P., *et al.* (2005) TRPC6 is a glomerular slit diaphragm-associated channel required for normal renal function. *Nat. Genet.* **37,** 739–744 CrossRef Medline
44. Heeringa, S. F., Möller, C. C., Du, J., Yue, L., Hinkes, B., Chernin, G., Vlangos, C. N., Hoyer, P. F., Reiser, J., and Hildebrandt, F. (2009) A novel TRPC6 mutation that causes childhood FSGS. *PLoS One* **4,** e7771 CrossRef Medline
45. Mottl, A. K., Lu, M., Fine, C. A., and Weck, K. E. (2013) A novel TRPC6 mutation in a family with podocytopathy and clinical variability. *BMC Nephrol.* **14,** 104 CrossRef Medline
46. Santín, S., Ars, E., Rossetti, S., Salido, E., Silva, I., García-Maset, R., Giménez, I., Ruíz, P., Mendizábal, S., Luciano Nieto, J., Peña, A., Camacho, J. A., Fraga, G., Cobo, M. A., Bernis C., *et al.* (2009) TRPC6 mutational analysis in a large cohort of patients with focal segmental glomerulosclerosis. *Nephrol. Dial. Transplant.* **24,** 3089–3096 CrossRef Medline
47. Lichtenegger, M., Tiapko, O., Svobodova, B., Stockner, T., Glasnov, T. N., Schreibmayer, W., Platzer, D., de la Cruz, G. G., Krenn, S., Schober, R., Shrestha, N., Schindl, R., Romanin, C., and Groschner, K. (2018) An optically controlled probe identifies lipid-gating fenestrations within the TRPC3 channel. *Nat. Chem. Biol.* **14,** 396–404 CrossRef Medline
48. Trebak, M., Hempel, N., Wedel, B. J., Smyth, J. T., Bird, G. S., and Putney, J. W., Jr. (2005) Negative regulation of TRPC3 channels by protein kinase C-mediated phosphorylation of serine 712. *Mol. Pharmacol.* **67,** 558–563 CrossRef Medline
49. Hasan, R., Leeson-Payne, A. T., Jaggar, J. H., and Zhang, X. (2017) Calmodulin is responsible for Ca^{2+}-dependent regulation of TRPA1 Channels. *Sci. Rep.* **7,** 45098 CrossRef Medline
50. Nilius, B., Prenen, J., Tang, J., Wang, C., Owsianik, G., Janssens, A., Voets, T., and Zhu, M. X. (2005) Regulation of the Ca^{2+} sensitivity of the nonselective cation channel TRPM4. *J. Biol. Chem.* **280,** 6423–6433 CrossRef Medline
51. Zheng, S. Q., Palovcak, E., Armache, J. P., Verba, K. A., Cheng, Y., and Agard, D. A. (2017) MotionCor2: anisotropic correction of beam-induced motion for improved cryo-electron microscopy. *Nat. Methods* **14,** 331–332 CrossRef Medline
52. Zhang, K. (2016) Gctf: real-time CTF determination and correction. *J. Struct. Biol.* **193,** 1–12 CrossRef Medline
53. Biyani, N., Righetto, R. D., McLeod, R., Caujolle-Bert, D., Castano-Diez, D., Goldie, K. N., and Stahlberg, H. (2017) Focus: the interface between data collection and data processing in cryo-EM. *J. Struct. Biol.* **198,** 124–133 CrossRef Medline
54. Rosenthal, P. B., and Henderson, R. (2003) Optimal determination of particle orientation, absolute hand, and contrast loss in single-particle electron cryomicroscopy. *J. Mol. Biol.* **333,** 721–745 CrossRef Medline
55. Emsley, P., and Cowtan, K. (2004) Coot: model-building tools for molecular graphics. *Acta Crystallogr. D Biol. Crystallogr.* **60,** 2126–2132 CrossRef Medline
56. Pettersen, E. F., Goddard, T. D., Huang, C. C., Couch, G. S., Greenblatt, D. M., Meng, E. C., and Ferrin, T. E. (2004) UCSF Chimera—a visualization system for exploratory research and analysis. *J. Comput. Chem.* **25,** 1605–1612 CrossRef Medline
57. Afonine, P. V., Grosse-Kunstleve, R. W., Echols, N., Headd, J. J., Moriarty, N. W., Mustyakimov, M., Terwilliger, T. C., Urzhumtsev, A., Zwart, P. H., and Adams, P. D. (2012) Towards automated crystallographic structure refinement with phenix.refine. *Acta Crystallogr. D Biol. Crystallogr.* **68,** 352–367 CrossRef Medline
58. Chen, V. B., Arendall W. B., 3rd, Headd, J. J., Keedy, D. A., Immormino, R. M., Kapral, G. J., Murray, L. W., Richardson, J. S., and Richardson, D. C. (2010) MolProbity: all-atom structure validation for macromolecular crystallography. *Acta Crystallogr. D Biol. Crystallogr.* **66,** 12–21 CrossRef Medline
59. Morin, A., Eisenbraun, B., Key, J., Sanschagrin, P. C., Timony, M. A., Ottaviano, M., and Sliz, P. (2013) Collaboration gets the most out of software. *Elife* **2,** e01456 CrossRef Medline